Journal of Sound and Vibration 642 (2026) 119919

Contents lists available at ScienceDirect

Journal of Sound and Vibration

journal homepage: www.elsevier.com/locate/jsvi

Locally resonant underwater lens for broadband waterborne sound focusing

Beomseok Oh [a], Dongwoo Lee [a,b], Yeon-Seong Choo [c], Sung-Hoon Byun [c], Jehyeon Shin [d], Sea-Moon Kim [c,*], Junsuk Rho [a,d,e,f,g,*]

[a] Department of Mechanical Engineering, Pohang University of Science and Technology (POSTECH), Pohang, 37673, Republic of Korea
[b] Naval Ship Performance R&D Team, Defense Technology R&D Center, Hanwha Ocean, Geoje, 3370, Republic of Korea
[c] Ocean and Maritime Digital Technology Research Division, Korea Research Institute of Ships & Ocean Engineering (KRISO), Daejeon, 34103, Republic of Korea
[d] Graduate School of Artificial Intelligence, Pohang University of Science and Technology (POSTECH), Pohang, 37673, Republic of Korea
[e] Department of Chemical Engineering, Pohang University of Science and Technology (POSTECH), Pohang, 37673, Republic of Korea
[f] Department of Electrical Engineering, Pohang University of Science and Technology (POSTECH), Pohang, 37673, Republic of Korea
[g] POSCO-POSTECH-RIST Convergence Research Center for Flat Optics and Metaphotonics, Pohang, 37673, Republic of Korea

ARTICLE INFO

Keywords:
Underwater acoustic lens
Locally resonant metamaterials
Cavity-based underwater lens
Lightweight underwater lens

ABSTRACT

Broadband underwater sound focusing in the low-frequency range is essential for various aquatic applications, particularly for long-range environmental monitoring and sensing. However, achieving lower-frequency focusing capability typically necessitates bulky, heavy structures that hinder practical deployment. Here, we introduce a three-dimensional underwater acoustic lens comprising cavity-based structures. By leveraging the local resonance nature of these structures, our approach effectively mitigates the wavelength-scale limitations of conventional Bragg scattering-based lenses, thereby enabling sound manipulation at substantially lower frequencies than achievable with comparably sized conventional counterparts. We experimentally validate its focusing performance over a frequency range of 20–35 kHz. Unlike conventional approaches that rely on fully filled structures, our design employs cavity-type, water-permeable scatterers, achieving efficient focusing with a remarkably lightweight structure. In addition, we observe that our lens exhibits asymmetric backscattering—a distinctive effect arising from its Willis coupling (bianisotropic) nature. With its cost-effective and subwavelength-scale design, the proposed lens provides a promising platform for underwater sensor networks and future advancements in on-demand waterborne sound focusing.

1. Introduction

The precise manipulation of underwater acoustic waves, particularly within the low-frequency range that includes the audible and lower-ultrasonic band, is essential for a wide range of applications, including sound navigation and ranging (SONAR), acquisition of oceanographic data, underwater communication, marine-pollution monitoring, and tactical surveillance [1–4]. Acoustic waves are more practical underwater owing to the significant attenuation of electromagnetic waves in aquatic environments [5,6]. From this perspective, controlling underwater acoustic energy is critical, for instance, in power-free sensor networks wherein batteries

* Corresponding authors.
E-mail addresses: bs.oh@postech.ac.kr (B. Oh), dwlee93@hanwha.com (D. Lee), chooys@kriso.re.kr (Y.-S. Choo), byunsh@kriso.re.kr (S.-H. Byun), jehyeon.shin@postech.ac.kr (J. Shin), smkim@kriso.re.kr (S.-M. Kim), jsrho@postech.ac.kr (J. Rho).

https://doi.org/10.1016/j.jsv.2026.119919
Received 30 January 2026; Received in revised form 22 May 2026; Accepted 26 May 2026
Available online 27 May 2026

have a limited capacity and are often not rechargeable [7]. However, this task is more challenging underwater than in air because underwater devices are vulnerable to harsh environmental conditions, such as fouling and corrosion. In this context, passive structure-based underwater sound focusing can play a crucial role in a wide range of applications, such as long-term deep-sea monitoring with wireless acoustic energy transfer, even under such extreme conditions. Recent advances in sound manipulation technologies using metamaterials and phononic crystals have enabled precise control of waves with high degrees of freedom [8–17]. Despite extensive research on adapting metamaterials for underwater sound manipulation [18–24], experimental demonstrations of three-dimensional lenses for low-frequency underwater focusing remain scarce. Notably, a significant milestone in this field was the first experimental realization of an acoustic gradient-index (GRIN) lens, which was not achieved until 2014 [25] and was enabled by advanced additive manufacturing techniques. Although Luneburg's seminal work in electromagnetics dates back to 1944 [26], its application in acoustics has only recently been realized. Over the past decade, various experimental implementations have emerged driving further advancements in the field of acoustics. Nevertheless, existing studies remain limited despite the significant potential in the low-frequency range and the necessity for aquatic applications, such as battery-free monitoring, ecological acoustic recording, and on-demand wireless power transfer. Most efforts have focused on two-dimensional lenses (or three-dimensional lenses in high-frequency regimes) [25], primarily because they require bulky structures, and experimental validation is more challenging underwater than in air. Additionally, the reliance on solid scatterer-based structures [27–35], which utilize Bragg scattering, contributes to the bulkiness of these systems, posing challenges for their practical implementation.

In this paper, we propose a lightweight three-dimensional underwater lens comprising cavity-resonant and water-permeable scatterers. Our lens demonstrates focusing performance in the lower ultrasonic range of 20–35 kHz, achieved by employing locally resonant structures with high spatial resolution, as opposed to conventional solid scatterer-based lenses. This approach enables a cost-effective and lightweight design, offering significant potential for practical lower-frequency underwater sound manipulation. Through comprehensive experimental validation and numerical simulations, we confirm the effectiveness of our lens design in achieving broadband and wide-angle focusing behavior. Moreover, the bianisotropic (pressure–velocity cross-coupling) properties [36–39] inherent in spatially asymmetric unit scatterers lead to asymmetric reflection characteristics. Consequently, we observe angle-invariant broadband focusing along with incidence-dependent backscattering. To the best of our knowledge, this study reports the first experimental realization of three-dimensional and wide-angle underwater focusing using locally resonant asymmetric building blocks, particularly in the lower-ultrasonic range. These results show that our approach can address the primary challenges pertaining to underwater lenses that are crucial for practical applications, namely, broadband operation, lens size and weight constraints, and robust signal-to-noise ratio (SNR) in submerged environments.

2. Design principle and characterization

2.1. Concept of the proposed underwater lens

A conceptual representation of this study is shown in Fig. 1(a). Our lens is characterized by broadband focusing in the lower ultrasonic regime, which is independent of the incidence direction, and asymmetric backscattering that varies with the angle of incidence within the lightweight structure. To realize these characteristics, we design a lens based on cavity-based water-permeable scatterers shaped similarly to Helmholtz resonators (Fig. 1(c)). By introducing spatially asymmetric structures instead of traditional symmetric scatterers (e.g., sphere, cube, and cross shapes), we induce the pressure–velocity cross-coupling known as bianisotropy or Willis coupling [36–40]. In particular, Helmholtz-resonator-like asymmetric building blocks typically exhibit propagation direction-independent transmission properties while featuring incidence-dependent reflection characteristics [37]. In this configuration, the acoustic cavity acts as a secondary scatterer that can be used to adjust the overall scattering response. Numerous previous studies have been conducted on electromagnetic, acoustic, and elastic bianisotropic metamaterials based on these characteristics [36–42]. Notably, our unit scatterers exhibit asymmetric reflection properties depending on the incident direction (left panel of Fig. 1(b)) while maintaining consistent, configuration-independent transmission characteristics, as indicated by the right panel of Fig. 1(b), where the phase difference remains close to zero. By incorporating these features into the lens design, we achieve consistent focusing performance regardless of the incidence direction, while observing distinct asymmetric backscattering induced by Willis coupling. Fig. 1(c) depicts the designed and fabricated lens for underwater sound focusing, along with the geometric details of the unit scatterers. Because water, the background medium, has a high acoustic characteristic impedance, we used stainless steel (STS 316L) as the base material. We then fabricated the lens as a monolithic structure using a laser power-bed fusion-based additive manufacturing process (see Appendix for details). The lens has a diameter of 240 mm and an operating frequency range of approximately 20–35 kHz.

Owing to the nature of the underwater environment, maximizing the contrast in the characteristic impedance between water and the unit cells is more challenging than in air. While bubble- or trapped-air-inclusion-based unit cells can achieve a large impedance contrast (and thus a high refractive index) [27,30,43], they are inherently more sensitive and vulnerable to environmental factors such as hydrostatic pressure and external loads. Moreover, these designs may suffer from excessive buoyancy and other practical constraints in real-world aquatic environments [43,44]. Given the harsh submerged conditions—such as high hydrostatic pressure and drag forces on ship-mounted platforms—constructing unit cells from high-density materials such as steel is more suitable for ensuring structural durability. Considering these factors, designing a high-index unit scatterer (similar to those used in optical and acoustic metamaterials for airborne applications) remains challenging in underwater environments. Consequently, a GRIN lens, which can provide broadband focusing with a relatively low-index distribution, is well-suited for underwater applications. Existing GRIN lenses have primarily been designed based on the Bragg scattering properties of phononic crystals; this implies that the period (or lattice constant) of each unit cell is inevitably close to the wavelength scale [27–33,35]. In real-world low-frequency applications

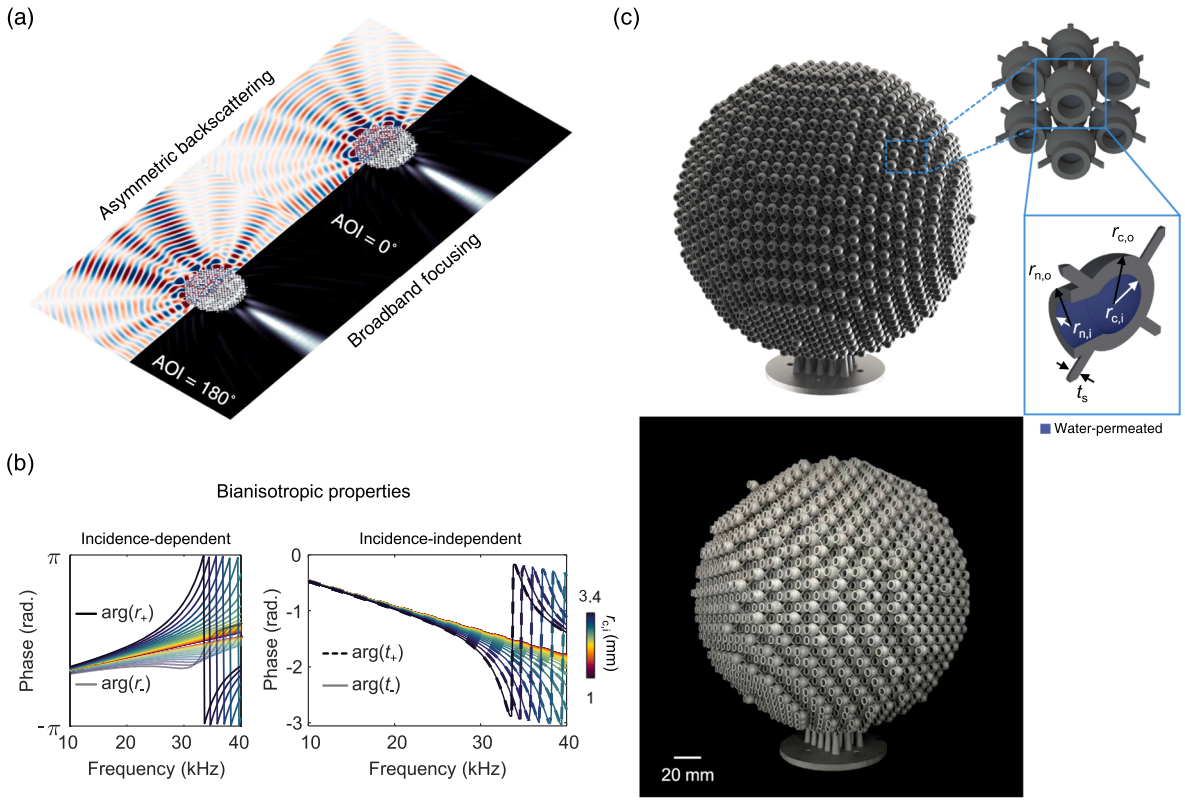

Fig. 1. Concept and principle of the proposed underwater lens. (a) Schematic of the proposed lens, featuring broadband underwater sound focusing and asymmetric backscattering attributed to pressure–velocity cross-coupling (i.e., Willis coupling). (b) Bianisotropic properties of cavity scatterers: Left, asymmetric reflection phase as a function of the geometric parameter (shown in (c)) and frequency. Right, incidence-independent transmission characteristics. The " + " and " - " symbols indicate incident angles of 0° and 180°, respectively. (c) Top, rendered images of the proposed lens. Each unit cell features an asymmetric geometry resembling a Helmholtz resonator. The geometric parameters include the radii of the outer and inner necks ($r_{n,o}$, $r_{n,i}$), the radii of the outer and inner cavities ($r_{c,o}$, $r_{c,i}$), and the thickness of connecting supporters (t_s). The water-permeated domain within a unit cell is highlighted in blue. Bottom, a photograph of the fabricated lens (scale bar: 20 mm; total diameter: 240 mm). (For interpretation of the references to colour in this figure legend, the reader is referred to the web version of this article.)

with constrained lens sizes, relatively large unit cells pose challenges for achieving an ideal continuous index profile. This limitation results in low spatial resolution and pronounced discreteness, leading to reduced focusing efficiency and parasitic diffraction [45]. This issue is related to impedance matching, wherein an increased number of layers reduces the intensity loss by enabling a more gradual change in the effective parameters.

2.2. Physical characterization of underwater scatterers

Our unit scatterers leverage locally resonant characteristics, as widely recognized in locally resonant metamaterials [46–49], rather than relying on conventional fully filled Bragg-based scatterers. In addition to the asymmetric geometry discussed previously, their deep subwavelength nature enables the lens to achieve the required effective index in the lower-frequency regime while maintaining high spatial sampling. Fig. 2(a) and (b) compare the effective refractive index of the proposed unit structures, compared with representative conventional metal-based solid scatterers: sphere, plus, and cube shapes, all designed with the same periodicity. The period $d = 0.01$ m, corresponding to approximately $0.18\,\lambda$ at the center frequency; this implies that each unit is deeply subwavelength. We can also consider air-inclusion-based bubble-like unit structures. However, to emulate a pressure-release boundary condition, the air inclusion must be encapsulated by a host shell whose characteristic impedance is close to that of water. This requirement constrains the host to low-impedance materials such as polymers and therefore compromises mechanical robustness, especially under harsh underwater loading conditions (e.g., high hydrostatic pressure). Accordingly, in this work we prioritize high-density materials and do not consider air-inclusion-based unit cells. Unlike conventional solid scatterers, cavity-type scatterers can achieve the desired refractive index in the lower-frequency range despite having a relatively small lattice constant. This fundamental difference arises from the distinct operating mechanisms of locally resonant versus Bragg scatterers. Conventional Bragg-type lattices operate on the first Bloch branch, where effective sound-speed modulation arises from approaching the band edge. The attainable refractive index at a fixed period increases with filling fraction, reaching its maximum as the unit-cell size approaches the period, requiring large filling fractions and operating at $ka \sim 1$. In contrast, the local resonance of Helmholtz resonators typically occurs at $ka \sim 0.3$ [50], enabling

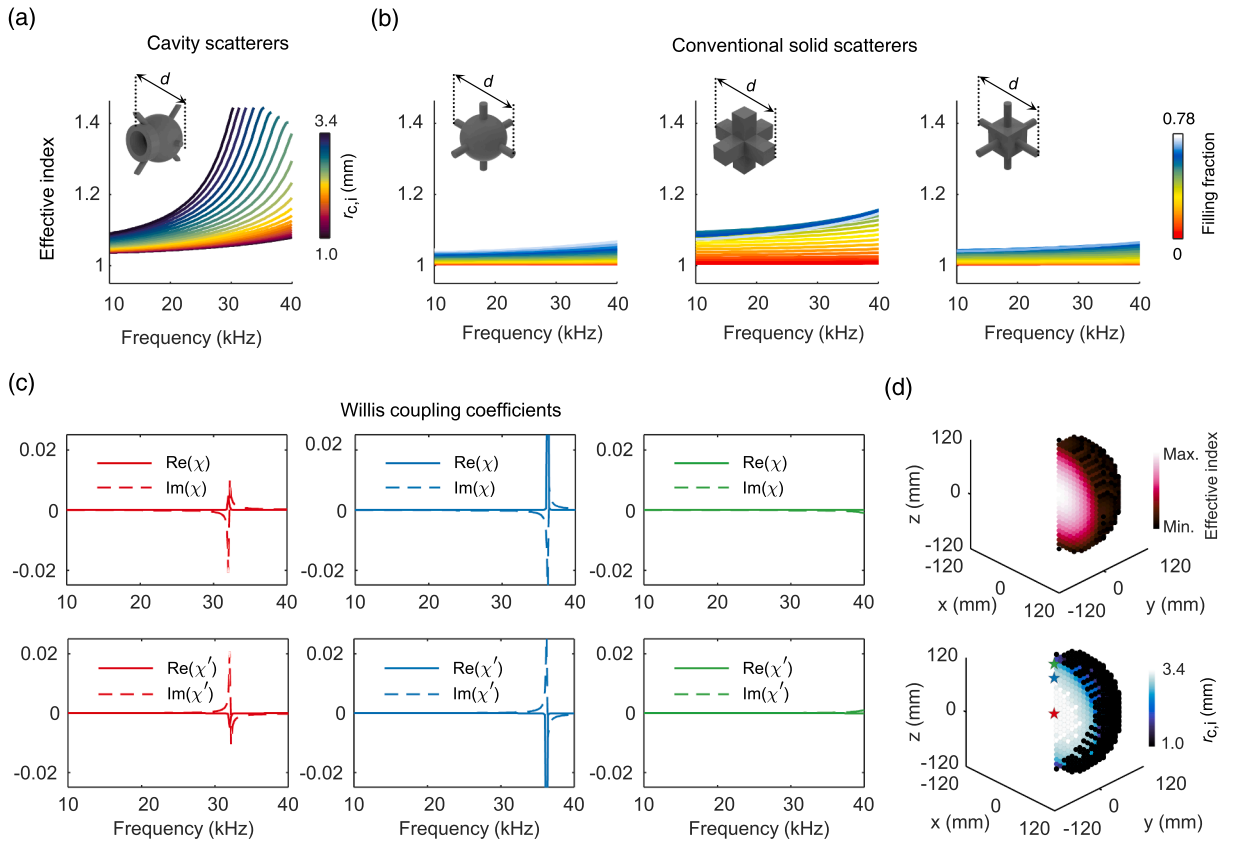

Fig. 2. Physical characterization of underwater scatterers. (a, b) Effective refractive indices for (a) the proposed scatterers and (b) conventional solid scatterers, including sphere (left), plus (middle), and cube (right) shapes. The parameter d represents the period of the unit structure, which is identical for all configurations. (c) Willis coupling coefficients of representative asymmetric scatterers, where geometrical parameters are indicated by star symbols in (d). (d) Effective index distribution of the designed lens (top) and corresponding geometrical parameters (bottom). The lens has a spherically symmetric profile, but only one-quarter of the structure is visualized here for clarity. The x-, y-, and z-axes represent the actual spatial coordinates in three-dimensional Cartesian space.

equivalent refractive indices with significantly smaller scatterers (see details below). This, in turn, leads to an increased focusing efficiency within the limited lens size, thereby enhancing the SNR in practical environments where background noise is inherently more prominent.

As mentioned above, our unit scatterers exhibit bianisotropic properties due to their spatial asymmetry. For a general Willis-coupled unit cell with a subwavelength lattice constant, the scattering properties can be understood as the coupling of an acoustic monopole and three orthogonal dipole moments [37]. This coupling can be fully described by a polarizability tensor or scattering matrix representation, which relates the incident pressure and particle velocity to the induced responses and plays a pivotal role in governing the proposed lens. Under plane wave incidence and assuming an implicit time-harmonic convention $e^{-j\omega t}$, the linear acoustic wave equation can be written as follows [37]:

$$\partial_z \begin{pmatrix} p \\ v \end{pmatrix} = \mathrm{j}k \begin{pmatrix} \chi & \rho \\ \beta & \chi' \end{pmatrix} \begin{pmatrix} p \\ v \end{pmatrix} \tag{1}$$

where k is the wavenumber, p is the acoustic pressure, v is the particle velocity, χ and χ' are the Willis coupling coefficients, and z denotes the propagation direction (angle-dependent notation omitted for simplicity). We note that conventional symmetric media have zero Willis coupling coefficients. In addition, for reciprocal bianisotropic unit scatterers (e.g., lossless Willis particles), $\chi = \chi'$. On the other hand, non-Hermitian asymmetric particles, such as those employing viscous-thermal boundary effects in narrow passages (particularly in ultrasonic regimes), may have $\chi \neq \chi'$, indicating that the effective medium has nonreciprocal responses. Given the subwavelength nature of the proposed cavity scatterers, the scattering can be regarded as emanating from a small portion of the effective medium characterized by a lattice constant d. In this case, by integrating Eq. (1) and utilizing the scattering (and/or transfer) matrix, we obtain the following Willis coupling coefficients:

$$\chi = -\frac{2\mathrm{j}}{\omega d} \frac{-1 + t_{11} - t_{12}t_{21} - t_{22} + t_{11}t_{22}}{1 + t_{11} - t_{12}t_{21} + t_{22} + t_{11}t_{22}},$$

$$\chi' = -\frac{2\mathrm{j}}{\omega d}\frac{-1 - t_{11} - t_{12}t_{21} + t_{22} + t_{11}t_{22}}{1 + t_{11} - t_{12}t_{21} + t_{22} + t_{11}t_{22}}, \tag{2}$$

where t_{kl} (k, l = 1, 2) are the elements of the transfer matrix $\mathbf{T}$. Under linear time-harmonic excitation, from the constitutive law, each scatterer has a constitutive matrix with effective parameters ρ, β, χ and χ'. Now we consider the propagation of a plane wave through an effective medium, which is formed by the periodic repetition of a unit structure with lattice constant d, where scattering occurs in small regions. Since numerical simulations yield the scattering matrix of each unit cell, while the effective constitutive parameters are extracted from the transfer matrix, we first establish the relations between the two representations. Using the transfer matrix representation, one can express the following relations,

$$\begin{pmatrix} p_2 \\ v_2 \end{pmatrix} = \begin{pmatrix} t_{11} & t_{12} \\ t_{21} & t_{22} \end{pmatrix} \begin{pmatrix} p_1 \\ v_1 \end{pmatrix}, \tag{3}$$

$$\begin{pmatrix} p_{2,\mathrm{f}} + p_{2,\mathrm{b}} \\ \rho c\left[p_{2,\mathrm{f}} - p_{2,\mathrm{b}}\right] \end{pmatrix} = \begin{pmatrix} t_{11} & t_{12} \\ t_{21} & t_{22} \end{pmatrix} \begin{pmatrix} p_{1,\mathrm{f}} + p_{1,\mathrm{b}} \\ \rho c\left[p_{1,\mathrm{f}} - p_{1,\mathrm{b}}\right] \end{pmatrix}, \quad \mathbf{T} = \begin{pmatrix} t_{11} & t_{12} \\ t_{21} & t_{22} \end{pmatrix}. \tag{4}$$

where the subscripts "f" and "b" denote "forward" and "backward" directions, respectively (indicating the forward and backward propagating pressure). From Eq. (4), we obtain the following two equations:

$$\begin{aligned} p_{2,\mathrm{f}} + p_{2,\mathrm{b}} &= t_{11}p_{1,\mathrm{f}} + t_{11}p_{1,\mathrm{b}} + Zt_{12}p_{1,\mathrm{f}} - Zt_{12}p_{1,\mathrm{b}}, \\ Zp_{2,\mathrm{f}} - Zp_{2,\mathrm{b}} &= t_{21}p_{1,\mathrm{f}} + t_{21}p_{1,\mathrm{b}} + Zt_{22}p_{1,\mathrm{f}} - Zt_{22}p_{1,\mathrm{b}}, \end{aligned} \tag{5}$$

$$\begin{aligned} p_{1,\mathrm{b}} &= p_{1,\mathrm{f}}\frac{Zt_{11} - Zt_{22} - t_{21} + Z^2t_{12}}{-Zt_{11} - Zt_{22} + t_{21} + Z^2t_{12}} + p_{2,\mathrm{b}}\frac{-2Z}{-Zt_{11} - Zt_{22} + t_{21} + t_{12}Z^2}, \\ p_{2,\mathrm{f}} &= p_{1,\mathrm{f}}\left[t_{11} + Zt_{12} + \left(t_{11} - Zt_{12}\right)\frac{Zt_{11} - Zt_{22} - t_{21} + Z^2t_{12}}{-Zt_{11} - Zt_{22} + t_{21} + Z^2t_{12}}\right] \\ &\quad + p_{2,\mathrm{b}}\left[\left(Zt_{12} - t_{11}\right)\frac{2Z}{-Zt_{11} - Zt_{22} + t_{21} + Z^2t_{12}} - 1\right], \end{aligned} \tag{6}$$

where Z is the free-space characteristic impedance $Z = \rho c$. From Eqs. (5) and (6), we obtain the scattering matrix $\mathbf{S}$,

$$\begin{aligned} \mathbf{S} &= \begin{pmatrix} s_{11} & s_{12} \\ s_{21} & s_{22} \end{pmatrix}, \\ s_{11} &= \frac{Zt_{11} - Zt_{22} - t_{21} + Z^2t_{12}}{-Zt_{11} - Zt_{22} + t_{21} + Z^2t_{12}}, \\ s_{12} &= \frac{-2Z}{-Zt_{11} - Zt_{22} + t_{21} + Z^2t_{12}}, \\ s_{21} &= \frac{2Z(t_{12}t_{21} - t_{11}t_{22})}{-Zt_{11} - Zt_{22} + t_{21} + Z^2t_{12}} \\ s_{22} &= \left(Zt_{12} - t_{11}\right)\frac{2Z}{-Zt_{11} - Zt_{22} + t_{21} + Z^2t_{12}} - 1. \end{aligned} \tag{7}$$

Finally, we obtain the relation between the transfer and scattering matrices by solving the inverse problem of Eq. (7) as follows,

$$\begin{aligned} t_{11} &= \frac{s_{22} - s_{11} - s_{11}s_{22} + s_{12}s_{21} + 1}{2s_{12}}, \\ t_{12} &= -\frac{s_{11} + s_{22} + s_{11}s_{22} - s_{12}s_{21} + 1}{2Zs_{12}}, \\ t_{21} &= \frac{Zs_{11} - Z + Zs_{22} - Zs_{11}s_{22} + Zs_{12}s_{21}}{2s_{12}}, \\ t_{22} &= \frac{s_{11} - s_{22} - s_{11}s_{22} + s_{12}s_{21} + 1}{2s_{12}}. \end{aligned} \tag{8}$$

Given the subwavelength nature of the proposed unit structures, the transfer matrix $\mathbf{T}$ can be approximated in the long wavelength regime ($\lambda \gg d$) based on the Padé approximation [51] as follows,

$$\begin{aligned} \mathbf{T} &= \left(\mathbf{I} - \mathrm{j}\frac{ckd}{2}\mathbf{\Gamma}\right)^{-1}\left(\mathbf{I} + \mathrm{j}\frac{ckd}{2}\mathbf{\Gamma}\right), \\ \mathbf{\Gamma} &= \begin{pmatrix} \chi & \rho \\ \beta & \chi' \end{pmatrix}, \end{aligned} \tag{9}$$

where $\mathbf{I}$ denotes the identity matrix. From Eq. (9), we finally obtain the effective parameters

$$\begin{aligned} \chi &= \frac{-2\mathrm{j}}{\omega d}\frac{-1 + t_{11} - t_{12}t_{21} - t_{22} + t_{11}t_{22}}{1 + t_{11} - t_{12}t_{21} + t_{22} + t_{11}t_{22}}, \\ \chi' &= \frac{-2\mathrm{j}}{\omega d}\frac{-1 - t_{11} - t_{12}t_{21} + t_{22} + t_{11}t_{22}}{1 + t_{11} - t_{12}t_{21} + t_{22} + t_{11}t_{22}}, \end{aligned}$$

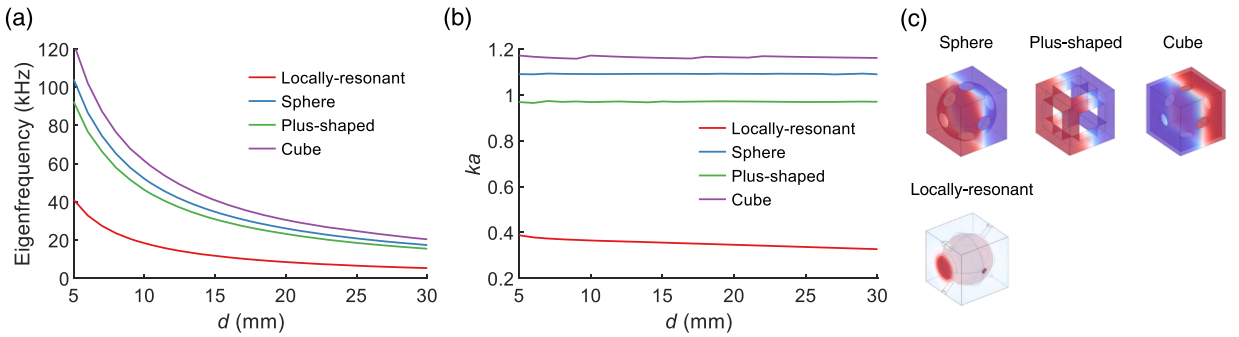

Fig. 3. Comparative analysis of unit cell characteristics. (a) Eigenfrequencies and (b) ka values as functions of unit cell period d for structures (locally resonant, sphere, plus-shaped, and cube) achieving $n \sim 1.4$. (c) Corresponding acoustic mode shapes: Bloch modes for Bragg-based structures (top) and resonance mode for the locally resonant structure (bottom).

$$\rho = \frac{4jt_{12}}{d\omega + dt_{11}\omega + dt_{22}\omega + dt_{11}t_{22}\omega - dt_{12}t_{21}\omega},$$
$$\beta = \frac{4jt_{21}}{d\omega + dt_{11}\omega + dt_{22}\omega + dt_{11}t_{22}\omega - dt_{12}t_{21}\omega}. \tag{10}$$

We can determine the constitutive parameters from the scattering parameters obtained through numerical simulations.

We represent the Willis coupling coefficients extracted from the scattering responses of representative cavity scatterers, as shown in Fig. 2(c), with their geometrical parameters indicated by star symbols in the bottom panel of Fig. 2(d). The full-wave simulations are conducted using a finite-element method based on the commercial software COMSOL MULTIPHYSICS 6.3, and we use the pressure acoustics and solid mechanics modules to realize acoustic-structure coupling calculations. To account for thermoviscous dissipation within the narrow passages of the unit cells, the narrow region acoustics feature was employed. For the thermoviscous acoustic modeling, we used the typical parameters of water including a specific heat ratio of 1.00, thermal conductivity of 0.58 $\mathrm{W/(m \cdot K)}$, heat capacity at constant pressure of 4.19 $\mathrm{kJ/(kg \cdot K)}$, and dynamic viscosity of 1.31×10^{-3} $\mathrm{Pa \cdot s}$. The mass density and sound speed of the background medium (water) are 999 $\mathrm{kg \cdot m^{-3}}$ and 1460 $\mathrm{m \cdot s^{-1}}$, respectively. The structure was assigned a mass density of 7980 $\mathrm{kg \cdot m^{-3}}$, a Young's modulus of 193 GPa, and a Poisson's ratio of 0.3. The real (imaginary) parts of each coefficient are represented by solid (dashed) lines. It is well known that each unit cell exhibits the most dispersive characteristics and its coupling coefficients reach maxima near the local resonance frequency. Therefore, it has pronounced asymmetric reflection characteristics, whereas the transmission remains unaffected by the spatially asymmetric configuration (as shown in Fig. 1(b)). This allows for the realization of effective index modulation independent of the incident direction for the lens design. Consequently, the Willis coupling governs the reflection (backscattering) channel of the lens while leaving the transmission-based focusing functionality unaffected, thereby enabling independent asymmetric backscattering control on top of the focusing performance. Moreover, the Willis coupling coefficients χ and χ' exhibit nearly identical values but opposite signs (Fig. 2(c)), that is, they have nearly reciprocal bianisotropic properties. This indicates that our system is nearly lossless owing to its low-frequency operation. By contrast, when thermoviscous losses become significant in the high-frequency regime, the system may exhibit nonreciprocal characteristics ($\chi \neq \chi'$). A detailed analysis of the viscous and thermal boundary-layer thicknesses, presented in Appendix C, confirms that the boundary layers are nearly three orders of magnitude smaller than the narrowest channel width at the maximum operating frequency, indicating that thermoviscous losses are negligibly small in the present system.

As discussed above, Bragg-type lattices and locally resonant scatterers operate through fundamentally different physical mechanisms, leading to distinct size-frequency constraints. Conventional Bragg structures rely on coherent scattering from periodic arrangements, operating on the first Bloch branch where sound-speed modulation emerges near the band edge. For these non-resonant systems, the achievable refractive index at a given period d scales with filling fraction, maximizing when the scatterer size approaches the lattice period—inherently constraining operation to $ka \sim 1$. In contrast, locally resonant Helmholtz resonators achieve dispersion through internal cavity resonances typically at $ka \sim 0.3$, smaller than the Bragg limit [50,52,53]. To quantify these differences, we analyze various unit structures designed to achieve $n \sim 1.4$, including solid scatterers (spheres, plus-shaped, cubes) and cavity-type resonators, all incorporating fabrication-compatible support structures (Fig. 3). For this comparison, solid scatterers require a high filling fraction of ~ 0.6 to reach the target index. In contrast, the Helmholtz resonators were configured with cavity dimensions of $r_{c,o} = d - 0.5\,\mathrm{mm}$, and $r_{c,i} = r_{c,o} - 0.3\,\mathrm{mm}$, representing near-maximum cavity volume within the period constraints. Fig. 3(a) and (b) present the eigenfrequencies and ka values as functions of unit-cell period, clearly demonstrating the distinct operating regimes between local resonance and Bragg scattering mechanisms, with the corresponding acoustic mode shapes shown in Fig. 3(c). Notably, at a 10 mm period, the cavity-based scatterers achieve an eigenfrequency of ~ 18.5 kHz, enabling lens designs at frequencies significantly lower than our design frequency of 31 kHz using the same physical footprint. This indicates that cavity-type scatterers with the same unit-cell period can operate at much lower frequencies than conventional designs. While our current implementation achieves operation at 0.18 λ without fully maximizing the cavity volume, the results demonstrate that even deeper subwavelength operation (potentially approaching 0.1 λ) is achievable through further optimization. This analysis provides quantitative evidence

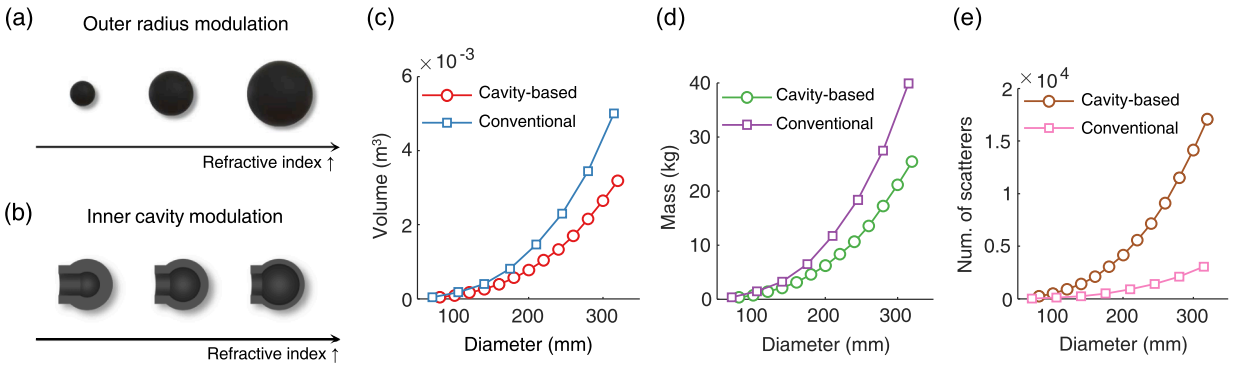

Fig. 4. Advantages of the proposed lens over conventional underwater lenses. (a, b) Schematic of refractive index modulation methods for (a) solid and (b) cavity-based scatterers. (c–e) Variation in the total volume (c), mass (d), and the number of unit scatterers (e) for the cavity-based and conventional lenses as a function of lens diameter. The cavity-based lens is significantly lighter, particularly at larger diameters, highlighting its weight reduction, cost, and scalability advantages.

that cavity-type lenses fundamentally overcome the size-frequency constraints of conventional Bragg-based designs. We would like to note that although our analysis focused on specific solid scatterer geometries, various other non-resonant solid scatterers remain fundamentally constrained by the size-frequency limit inherent to Bragg scattering.

2.3. Design of the lens

Without loss of generality, we design a spherical lens with a diameter of 240 mm by using the index profile of a generalized spherically symmetric lens, described by $n(r) = \sqrt{R^2 - r^2 + f^2}/f$, where R is the radius of the lens, and f is the focal length. The design is based on a reference frequency of 31 kHz. We set the focal length to 0.2 m to prevent the focus from forming on the lens surface and for experimental verification. The desired effective index distribution and corresponding geometrical parameters are shown in Fig. 2(d). Notably, the proposed scatterers with resonance frequencies closer to the reference frequency are arranged nearer to the center of the lens. In addition, asymmetric backscattering is expected to be primarily governed by unit structures with strong pressure–velocity coupling, which are also located closer to the center of the lens.

2.4. Advantages of the cavity-based lens over conventional GRIN lenses

Because Bragg scattering inevitably occurs at higher frequencies, conventional GRIN lenses inherently require a larger lattice constant than the proposed lens, which is local-resonance-based. This results in a lower spatial resolution or lower discretization levels, consequently reducing the focusing efficiency [45]. Moreover, while cavity-based scatterers can maintain consistent outer geometrical parameters ($r_{c,o}$, $r_{n,o}$), solid scatterers require larger geometrical parameters and consequently higher effective refractive indices as they approach the center of the lens, leading to an increased filling fraction approaching unity [25]. Furthermore, to ensure the overall structural stability of the lens, the size of the supporters connecting the unit cells must be increased, ultimately leading to an increase in the total mass.

Fig. 4 depicts the changes in the volume and mass of a conventional (sphere-based) lens and a cavity-based lens as a function of the diameter designed for the same reference frequency. In this comparison, the lattice constant of a conventional lens is set to 17.5 mm, which is 1.75 times that of the cavity-based lens. Remarkably, for a lens diameter of 280 mm, the cavity-based lens, despite comprising a larger number of unit cells—11,513 compared to 2109 in the conventional design—is approximately 1.6 times (nearly 40 %) lighter. In particular, the conventional lens weighs 27.5 kg, whereas the proposed lens weighs only 17.2 kg (Fig. 4(d)). This weight reduction is attributed to the design strategy in which only the inner volume of each unit is adjusted to achieve different refractive indices. By contrast, the outer geometrical parameters remain unchanged, resulting in a lightweight structure without compromising spatial resolution (Fig. 4(a), (b)). Furthermore, the volume and mass differences between the conventional and cavity-based lenses become even more pronounced as the lens size increases. These results highlight the advantages of the proposed lens architecture, which enables higher spatial resolution—leading to more efficient focusing with reduced parasitic diffraction—and significantly reduces weight and material usage. We also note that the appropriate lens size can be selected based on the desired focusing gain and bandwidth.

3. Results and discussion

3.1. Experimental and numerical verification of underwater sound focusing

In Fig. 5, we present the entire experimental setup used for the acoustic measurements conducted in the water tank. The system consists of a scanning frame mounted on the rail platform (Fig. 5(a)), with an omnidirectional transducer mounted on a vertical

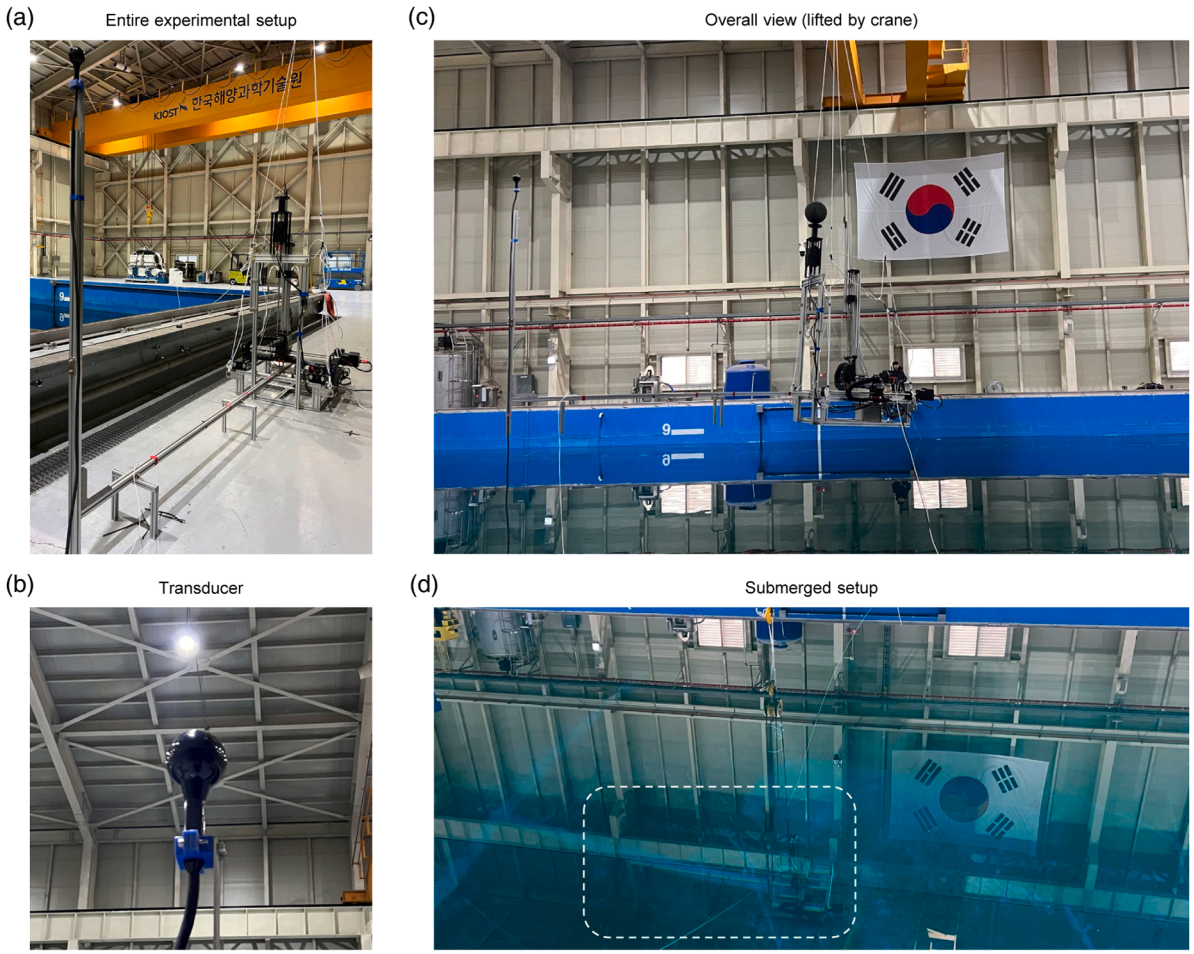

Fig. 5. Photographs of the overall experimental setup. (a) Full view of the entire acoustic measurement system. (b) Close-up image of the omnidirectional transducer mounted on the vertical support rod. (c) Side view of the setup lifted by an overhead crane. (d) A photograph of the submerged setup, with the region indicated by the white dashed box.

support rod for signal excitation (Fig. 5(b)). A crane-assisted view of the setup is shown in Fig. 5(c), illustrating the alignment of the device above the water. For actual measurements, the setup is fully submerged, as shown in Fig. 5(d). The measurements were conducted in a large water tank ($35 \times 20 \times 9.6$ m^3). The lens was fabricated as a monolithic structure by using additive manufacturing technology. The sample was fabricated using a metal additive printer (Concept Laser M2 Cusing; GE Additive). The base powder used for lens fabrication was STS 316L, which offers resistance to rust and degradation, even in saline or harsh underwater environments. Lens supporters are affixed to the underside of the lens to ensure proper integration with the measurement system. After completing the structure printing, various post-processing steps were performed, including laser cutting, hot isostatic pressing, and other treatments designed to improve the overall quality and structural reliability of the fabricated sample. We also analyzed the surface roughness of the sample using confocal microscopy (OPTELICS Hybrid; Lasertec). The measured mean surface roughness is 8.23 μm. A comprehensive description of these measurements, along with a discussion on the impact of surface roughness on potential losses, is provided in the Appendix. Furthermore, the Appendix includes photographs of the fabricated lens and further details regarding its mechanical characterization.

In the right panel of Fig. 6(a), we show a photograph of the fabricated lens mounted on the experimental setup. The input waves were generated using an omnidirectional transducer, and the lens was positioned 2.7 m away from the source to ensure the plane-wave incidence. A hydrophone scanned the measurement plane near the focal point using point-by-point measurements with a three-dimensional automatic linear stage. A rotational stage was used for measurements at several incident directions. The dimensions of the measurement area were 0.2×0.3 m^2, and the pixel size is 0.01×0.01 m^2 (approximately $0.18\ \lambda \times 0.18\ \lambda$ based on the center frequency of 27.5 kHz). Prior to characterizing the focusing field of the lens, we experimentally validated the successful generation of plane waves from the transducer radiation across multiple frequencies (20, 25, 30, 33, and 35 kHz). The measured phase distributions without the lens, presented in Appendix D (Fig. D.1(a)), confirm uniform wavefront propagation at the lens position, verifying the plane-wave incidence assumption.

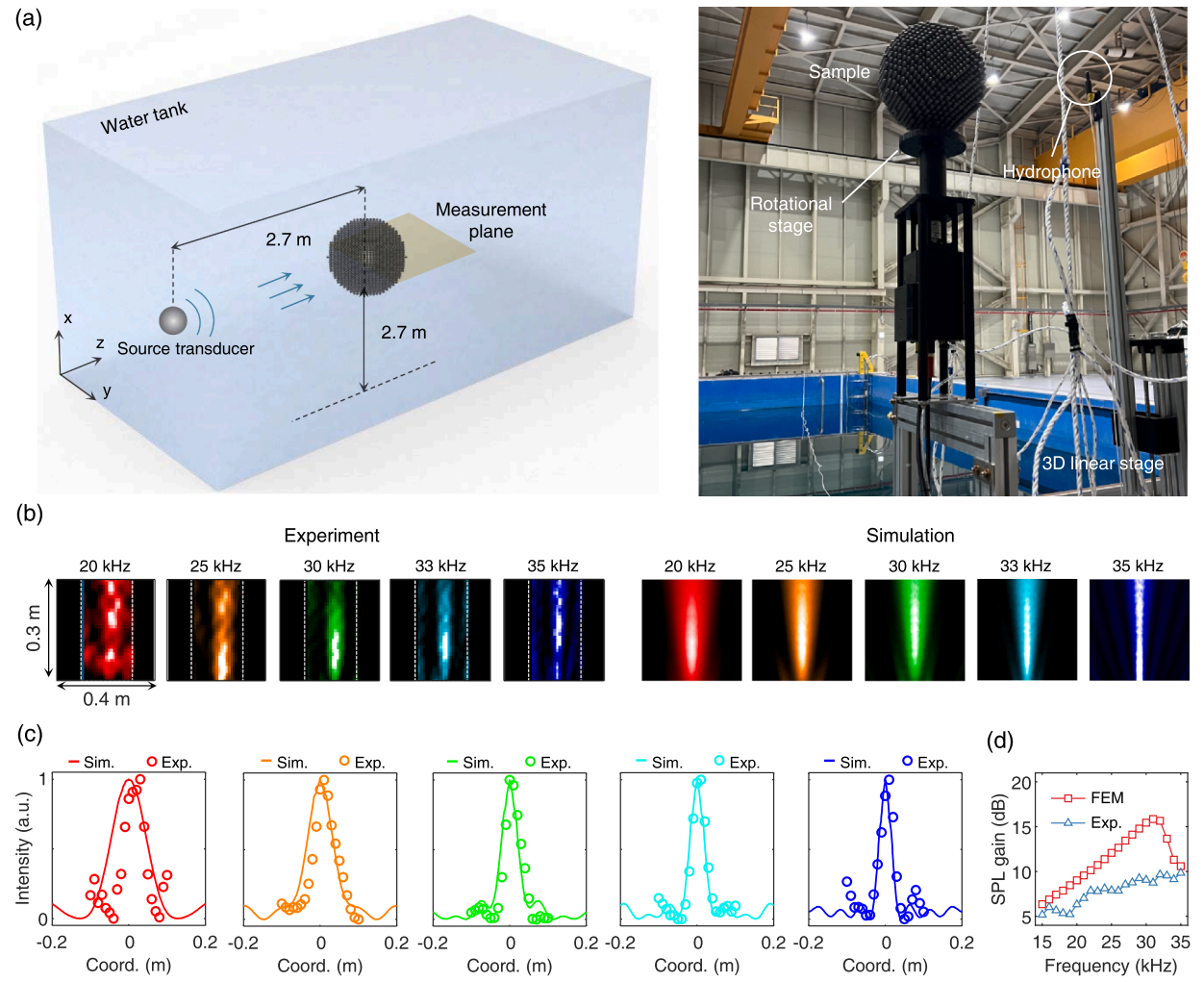

Fig. 6. Experimental validation of broadband underwater sound focusing. (a) Schematic (left) and photograph (right) of the experimental setup. (b) Experimental (left panels) and numerical (right) intensity fields of the fabricated lens in the $y - z$ plane at various frequencies indicated at the top. The incident wave propagates along the z-axis. (c) One-dimensional point spread functions (PSFs) obtained from experimental (markers) and numerical (solid lines) results. (d) Simulated and measured sound pressure level (SPL) gain as a function of frequency. The gain is defined as the ratio of the SPL at the focal point to that at the lens position without the lens.

The fabricated sample was submerged by a hoist system. An omnidirectional projector (ITC-1042; frequency range 0.01 to 100 kHz; International Transducer Corporation) was placed at 2.7 m in front of the lens to generate incident plane waves. The input signal was applied to the projector using an arbitrary waveform generator (PXI-5421; National Instruments) and a power amplifier (Type 2713; Brüel & Kjær). For signal transmission, a series of burst tones within the 20–35 kHz frequency range was employed. To perform sound field scanning at the measuring planes, a hydrophone (Type 8103; Brüel & Kjær) was employed. After calibration with a hydrophone calibrator (Type 4229; Brüel & Kjær), the hydrophone was mounted on an automated 3D positioning system and used as the receiver to detect and record acoustic pressure with high precision. The scanning resolution was set to 1 cm, with a 2 s interval between each measurement. The output acoustic signals were conditioned by a charge amplifier (Type 2692; Brüel & Kjær).

For numerical field analysis, three-dimensional finite element simulations were performed. To reduce computational cost, a half-symmetry model was employed by applying a symmetry boundary condition along the vertical mid-plane of the lens. The computational domain consisted of a half-cylindrical water region surrounding the lens structure. Plane wave excitation was introduced through a background pressure field imposed over the entire domain. To suppress spurious reflections at the domain boundaries, a perfectly matched layer (PML) boundary condition was applied along the curved outer surface of the half-cylindrical domain, absorbing outgoing waves and emulating an unbounded medium. On the top and bottom flat faces of the cylindrical domain, plane wave radiation conditions were imposed to allow free-field wave propagation along the axial direction. This combination of boundary treatments ensured simulation accuracy while maintaining computational efficiency.

Fig. 6(b), (c) show the measured and calculated acoustic intensity distributions of the lens at a 0° angle of incidence (AOI). Overall, good agreement is observed between the captured and calculated results, demonstrating broadband focusing performance. Fig. 6(d)

Table 1
Comparison of representative underwater GRIN lenses.

Reference	Mechanism	Dimension	Operating frequency[a]
Su *et al.* (2017) [54]	Bragg	2D	20–45 (kHz)
Ruan *et al.* (2019) [55]	Bragg	2D	15–25 (kHz)
Allam *et al.* (2020) [27]	Bragg	3D	~100 (kHz)
Li *et al.* (2021) [30]	Bragg	3D	~1 (MHz)
Kim *et al.* (2022) [28]	Bragg	3D	60–160 (kHz)
Tong & Ren (2023) [35]	Bragg	3D	30–38 (kHz)
Lee *et al.* (2025) [34]	Bragg	2D	120–150 (kHz)
This work	Local resonance	3D	20–35 (kHz)

[a] Based on the experimentally validated frequency range reported in each reference.

further presents the simulated and measured SPL gain as a function of frequency. Although some deviations exist between the two curves, the measurements follow an overall trend similar to that of the simulation across the operating band, confirming broadband focusing in terms of intensity enhancement at the focal point. The differences between the experimental and simulated results may be attributed to fabrication errors in the sample and undesired scattering caused by the experimental setup. Notably, the lens maintains broadband focusing performance owing to the incidence-independent characteristics of our scatterers. This can be largely attributed to the three-dimensional nature of the proposed lens, which significantly outperforms conventional low-frequency underwater lenses [54,55]. A concise comparison with representative underwater GRIN lenses is summarized in Table 1, highlighting that the proposed lens achieves broadband 3D focusing in the low-frequency regime through a local-resonance-based mechanism. Furthermore, the 3D focusing capability suggests that the proposed lens can achieve a higher SNR in submerged environments where ambient noise is dominant, making it a highly effective solution for practical applications.

3.2. Wide-angle focusing with asymmetric scattering characteristics

We now investigate two key features: incidence-dependent asymmetric backscattering and incidence-independent wide-angle focusing. Fig. 7(a) shows the measured one-dimensional PSFs at 25, 30, 33, and 35 kHz. As discussed above, our lens exhibits incidence-independent transmission and incidence-dependent reflection responses. Therefore, we observe that, regardless of the incidence direction, the lens maintains consistent focusing field distributions, making it suitable for wide-field underwater focusing. Fig. 7(b) presents the simulated scattered fields for 0° and 180° incidence at each frequency, clearly illustrating the asymmetric backscattering behavior. As previously discussed, cavity-based scatterers exhibit asymmetric reflection phases across the entire operational frequency range, with each scatterer reaching maximum Willis coupling near its local resonance frequency. Consequently, asymmetric backscattering responses were observed across a wide frequency range.

3.3. Potential of asymmetric backscattering field manipulation

Now we expand the design space of cavity scatterers beyond the limited geometric configurations used for the GRIN lens above, exploiting the additional degrees of freedom to investigate the potential for realizing versatile control of backscattering fields. To explore the impact of Willis coupling on scattering behavior, we analyze and compare a set of selected representative scatterers under two configurations: one exhibiting Willis coupling (asymmetric design) and another with zero Willis coupling, i.e., symmetric sphere scatterers (Fig. 8(a), (b)). For the sphere scatterers, we vary the filling fraction, whereas for the asymmetric scatterers we jointly tune four geometric parameters, $(r_{c,o},\, r_{n,o},\, r_{c,i},\, r_{n,i}) \in \left[d/5,\, d/2 - d/20\right]^4$, where $\Delta r_c \equiv r_{c,o} - r_{c,i} \geq 0.5\,\text{mm},\ \Delta r_n \equiv r_{n,o} - r_{n,i} \geq 0.5\,\text{mm}$.

We design GRIN structures of radius $R = 100$ mm, referenced at 33 kHz, that preserve transmission-based GRIN focusing while enabling both asymmetric and symmetric backscattered fields (Fig. 8(c)–(f)). To realize this, we adopt a strategy that jointly assigns unit-cell types and orientations from a reduced basis. An 11-member representative basis is selected and placed across the full 3D configuration. Unlike planar metasurfaces, reflection from a GRIN structure is intrinsically complex, arising from multiple internal reflections and interference, which renders direct library-based forward design ill-posed. While optimization could in principle address this challenge, it requires numerous sequential iterations of computationally expensive full-wave 3D simulations. Instead, we employ a data-driven combinatorial screening approach, in which hundreds of admissible assignments consistent with the generalized Luneburg profile for transmitted focusing are generated and evaluated in parallel on a lab-built cluster. More specifically, the background domain is configured as a cylindrical geometry with a radius of 0.25 m and height of 0.5 m. To ensure numerical accuracy, we employ a fine physics-controlled mesh consisting of $\sim 7 \times 10^7$ tetrahedral elements, providing at least $\sim$ 6–8 elements per wavelength in all media. In particular, the design space is restricted as follows: $r_{c,o} \in \{2.5, 3.0, 3.5, 4.0, 4.5\}$ mm, $r_{n,o} \in \{2.0, 2.5, 3.0, 3.5, 4.0\}$ mm, while $r_{c,i}, r_{n,i}$ are varied with a step size of 0.1 mm within the admissible ranges. Direct forward design of a 3D GRIN structure for specific backscattering fields is challenging due to multiple internal reflections/scatterings and interference within the structure. Moreover, the computational cost is significant; for example, analyzing a structure of $R = 100$ mm requires a large amount of memory. Therefore, instead of pursuing an iterative and computationally prohibitive optimization process, we adopt a combinatorial screening strategy. Specifically, we generate hundreds of admissible configurations that (i) satisfy the generalized spherically symmetric lens profile and

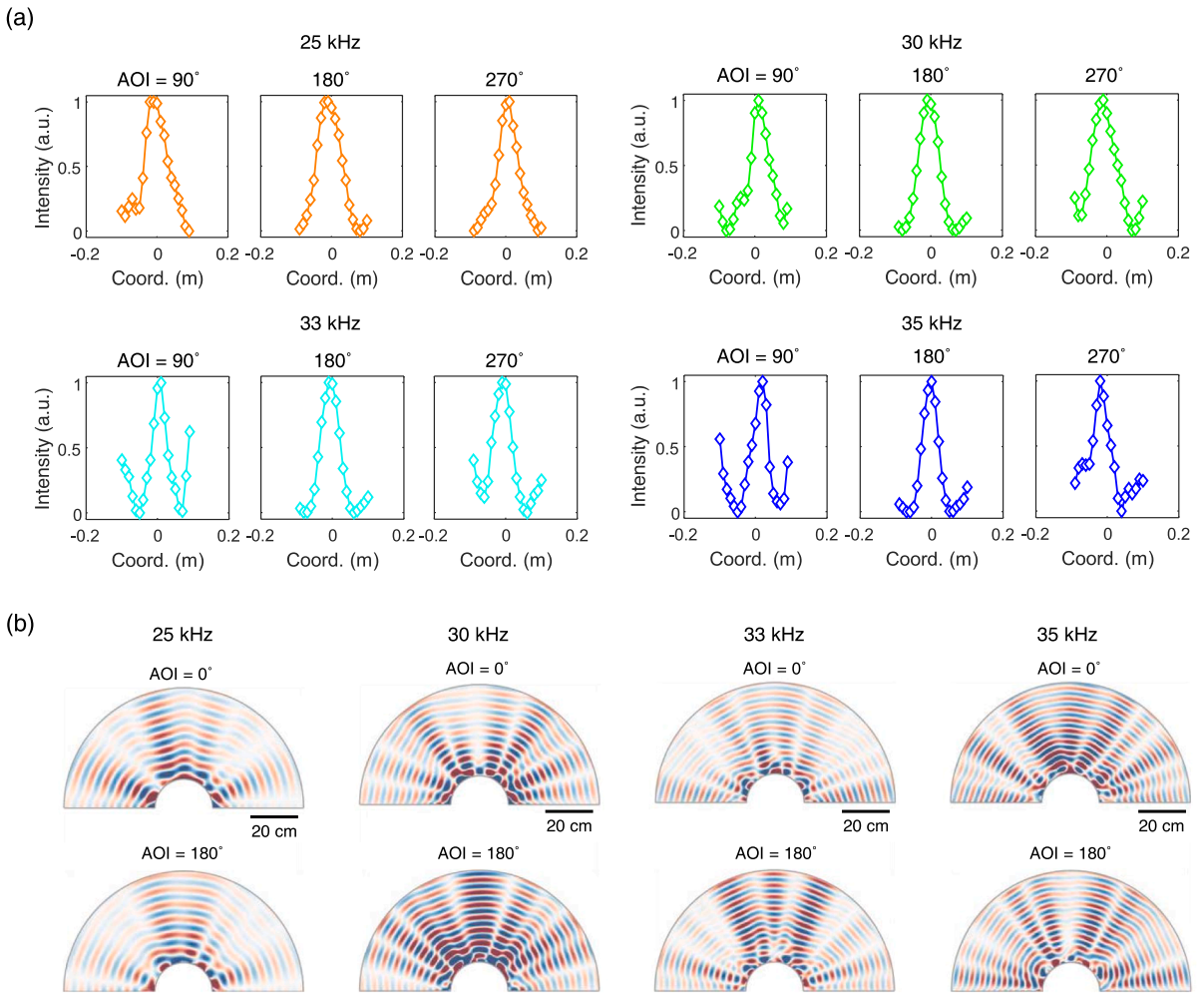

Fig. 7. Incidence-dependent and -independent characteristics of the lens. (a) Measured intensity profiles for AOIs of 90°, 180°, and 270°, and frequencies of 25, 30, 33, and 35 kHz. (b) Asymmetric backscattering fields for different incidence directions. For 0° AOI, the neck region of the cavity scatterer points toward the propagation direction, while at 180°, the direction is reversed. The scale bar represents a length of 20 cm.

Table 2
Detailed geometrical parameters of GRIN structures.

Case 1 (#)	1	2	3	4	5	6	7	8	9	10	11
$r_{c,i}$ (mm)	2.50	3.30	3.30	2.90	2.20	2.20	3.00	2.70	2.60	2.10	1.10
$r_{c,o}$ (mm)	4.00	4.00	4.00	3.50	3.50	3.50	4.00	4.00	4.00	4.00	3.00
$r_{n,i}$ (mm)	2.00	2.00	2.00	1.70	1.50	1.50	2.00	1.70	1.70	1.70	2.10
$r_{n,o}$ (mm)	2.50	2.50	2.50	3.00	3.00	2.50	2.50	2.50	3.00	2.50	2.50
Case 2 (#)	1	2	3	4	5	6	7	8	9	10	11
$r_{c,i}$ (mm)	3.50	3.50	2.50	2.60	3.50	3.00	2.50	2.90	2.90	1.80	2.10
$r_{c,o}$ (mm)	3.50	3.50	3.00	3.50	4.00	3.50	3.00	3.50	3.50	3.00	4.00
$r_{n,i}$ (mm)	1.90	1.90	1.40	1.50	2.50	2.00	1.50	2.10	2.50	1.00	1.90
$r_{n,o}$ (mm)	2.50	2.50	2.50	2.00	3.00	3.00	3.00	3.00	3.00	2.00	2.50

(ii) draw unit-cell types from the 11-member representative basis. All candidates are then simulated in parallel on a computing cluster to enable efficient evaluation and analysis.

Among the diverse realizable wavefield patterns, we select two representative backscattered field targets—focusing/splitting and focusing/focusing—demonstrating that the extended design space enables not only asymmetric but also nearly symmetric backscattered responses (Fig. 8(c), (d)). The geometrical parameter combinations of the GRIN structure presented in Fig. 8 of the main text are detailed in Table 2.

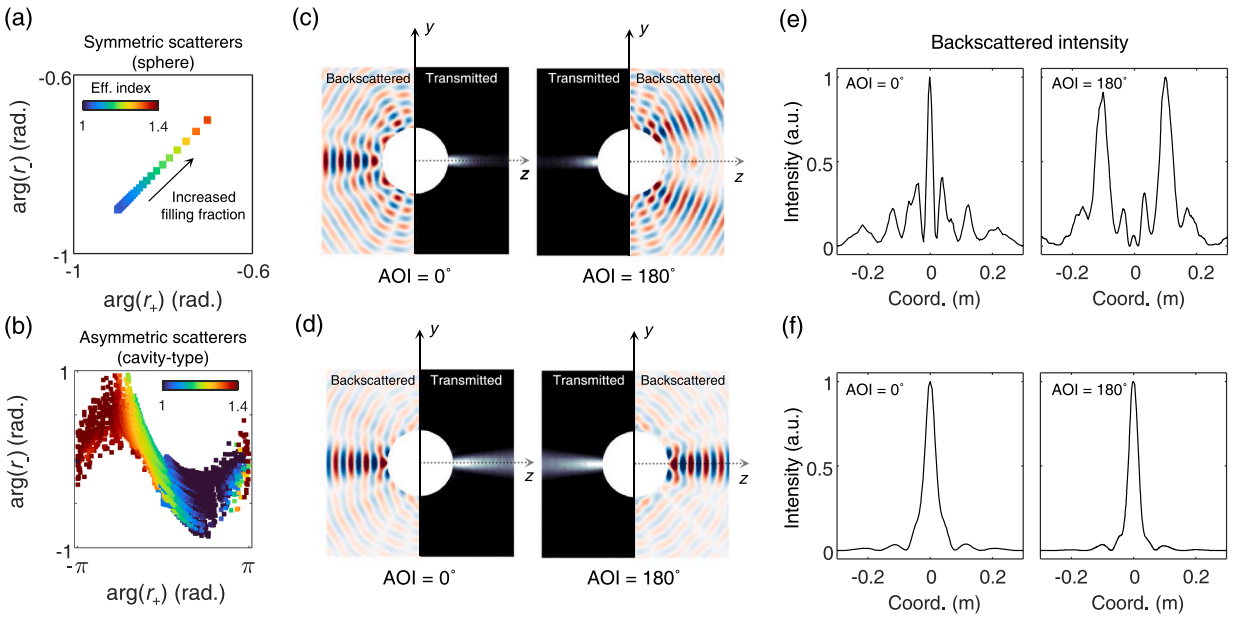

Fig. 8. Tailored transmitted and backscattered fields with asymmetric scatterers. (a) Reflection phase trajectory of sphere scatterers (symmetric) with respect to the effective refractive index. The " + " and " - " symbols indicate AOIs of 0° and 180°, respectively. (b) Reflection phase trajectory of cavity-type asymmetric scatterers with extended geometric degrees of freedom (jointly tuned $r_{c,o}$, $r_{n,o}$, $r_{c,i}$, $r_{n,i}$), showing distinct forward and backward phase responses depending on the incidence direction. (c–f) Simulated field distributions and backscattered intensity profiles of GRIN structures designed with cavity-type asymmetric scatterers. Asymmetric case: focusing at AOI = 0° and beam splitting at AOI = 180° (c), symmetric case: focusing for both AOI = 0° and 180° (d). Corresponding backscattered intensity profiles for focusing/splitting case (e), and focusing/focusing case (f).

We also note that, for complex GRIN structures, achieving precise and efficient control of the backscattered field over a wide frequency range remains an open problem and a promising avenue for future work.

4. Conclusions

We devised a new underwater acoustic lens that moves beyond traditional solid scatterer-based approaches and provides an efficient solution for practical applications. Our results expand the accessible low-frequency range, including the audible and lower-ultrasonic spectrum, which becomes increasingly significant in submerged environments. Experiments further confirm the focusing performance under realistic conditions. Importantly, the proposed lens achieves significant weight reduction, underscoring its potential for real-world deployment. We also examined the potential of cavity-type asymmetric scatterers, showing that their bianisotropic nature enables asymmetric responses arising from spatially asymmetric configurations. This highlights the further possibility of dual-functionality designs that leverage the complex multiple scattering characteristics of GRIN structures for precise control of backscattered fields. In this sense, the present study serves as a starting point for further investigations that will lead to the development of robust platforms for on-demand waterborne sound focusing and their integration into underwater wireless sensor networks. Additionally, the unique characteristics of underwater environments, especially the potential for fluid-structure interactions, may offer further opportunities to increase the degrees of freedom in wave manipulation. Future extensions of this platform may incorporate advanced designs that account for non-local interactions among unit scatterers, leading to more efficient and versatile acoustic focusing in GRIN metamaterial applications. Future research should address the acoustic (dynamic) properties and structural (static) characteristics, including varying hydrostatic pressures at different submerged depths and drag forces from ocean currents during vessel maneuvers. This integrated consideration of dynamic and static factors will provide a solid foundation for underwater lens design, marking a promising direction for future studies.

CRediT authorship contribution statement

Beomseok Oh: Writing – original draft, Visualization, Methodology, Investigation, Formal analysis, Data curation; **Dongwoo Lee:** Methodology, Investigation; **Yeon-Seong Choo:** Validation; **Sung-Hoon Byun:** Methodology, Investigation, Funding acquisition; **Jehyeon Shin:** Methodology, Investigation; **Sea-Moon Kim:** Writing – review & editing, Validation, Supervision, Resources, Project administration, Funding acquisition; **Junsuk Rho:** Writing – review & editing, Validation, Supervision, Resources, Project administration, Funding acquisition, Conceptualization.

Data availability

Data will be made available on request.

Declaration of competing interest

The authors declare that they have no known competing financial interests or personal relationships that could appear to influence the work reported in this paper.

Acknowledgment

This work was financially supported by the POSCO-POSTECH-RIST Convergence Research Center program funded by POSCO; the National Research Foundation (NRF) grant (RS-2024-00356928) funded by the Ministry of Science and ICT (MSIT) of the Korean government, and the grant (PES5550) from the endowment project of "Development of smart sensor technology for underwater environment monitoring" funded by Korea Research Institute of Ships & Ocean Engineering (KRISO). B.O. acknowledges the NRF Ph.D. fellowship (RS-2024-00409956) funded by the Ministry of Education (MOE) of the Korean government, and the POSTECH Alchemist fellowship. J.S. acknowledges the Hyundai Motor Chung Mong-Koo Foundation; the Institute of Information & Communications Technology Planning & Evaluation (IITP) (RS-2019-II191906, the POSTECH Artificial Intelligence Graduate School program) funded by the MSIT of the Korean government; the NRF Ph.D. fellowship (RS-2025-25438817) funded by the Ministry of Education (MOE) of the Korean government.

Appendix A. Fabrication of the lens

As described in the main text, the sample was fabricated using a metal additive manufacturing method. Fig. A.1 presents various views of the fabricated lens. The pillar and circular flange-like structures at the base of the lens were designed for mechanical integration with the experimental apparatus. In Fig. A.2, we show images of the lens immediately after printing, prior to post-processing. The lens structure was layered such that the neck of the Helmholtz resonator was oriented against gravity. Subsequently, the column-shaped supporters formed at the base were removed using laser cutting.

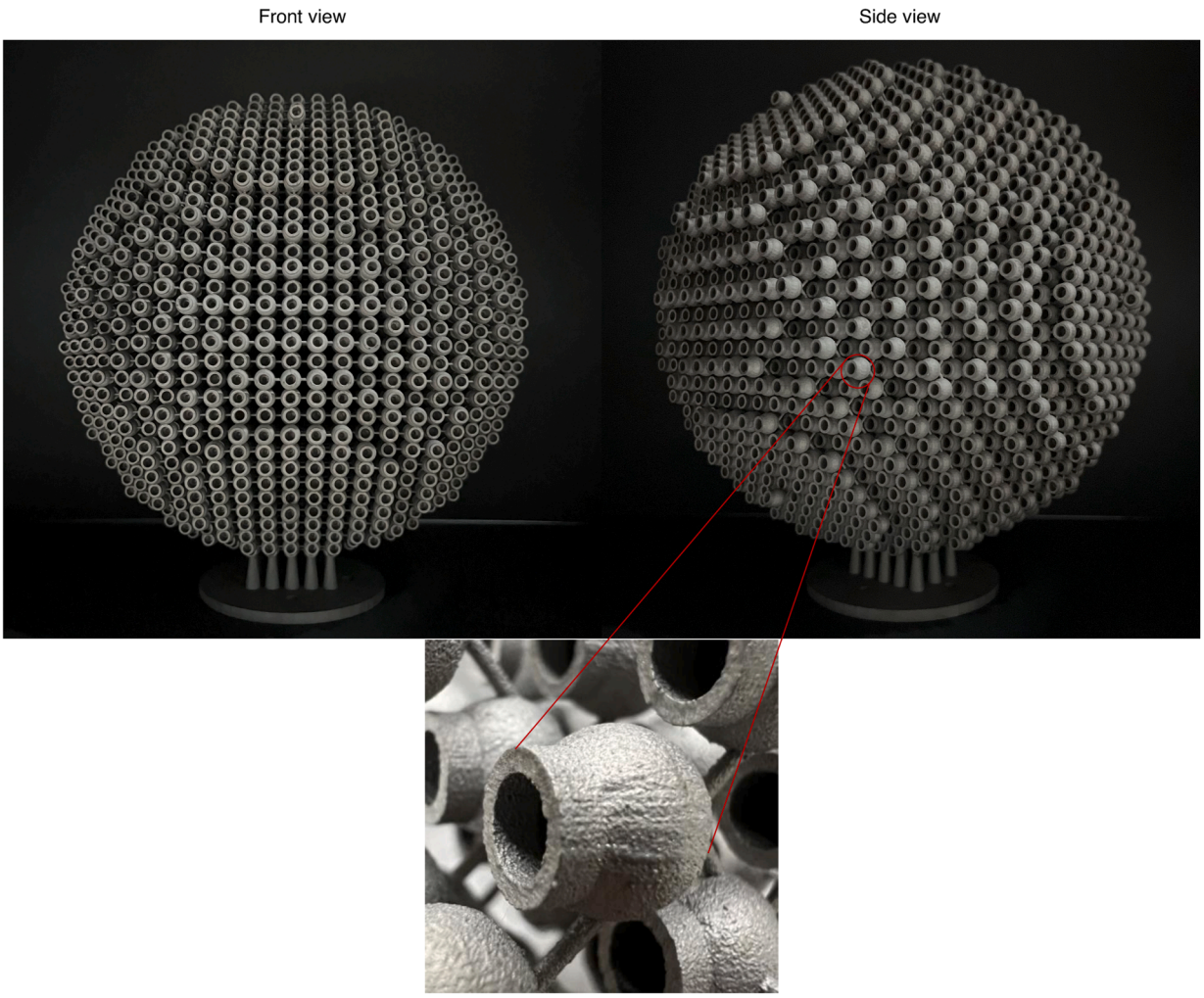

Fig. A.1. Photographs of the fabricated lens.

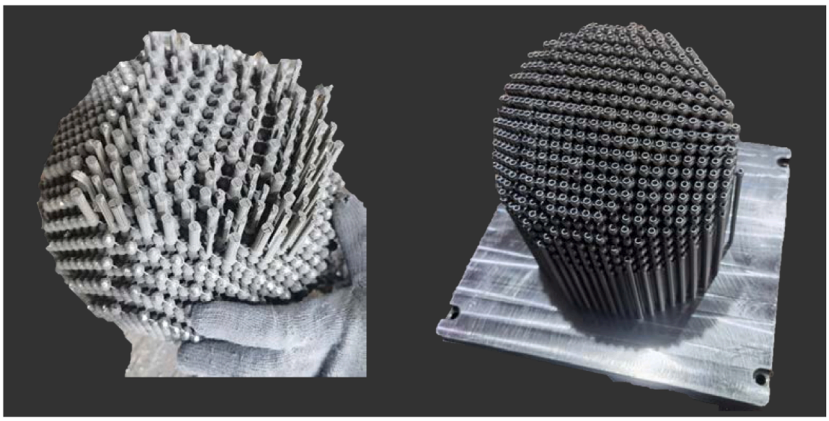

Fig. A.2. Snapshots of the fabricated lens before post-processing. Immediately after being printed on the bed (right) and prior to removing the base supports using laser cutting (left).

Appendix B. Mechanical testing of the additively manufactured specimen

To verify whether the fabricated lens structure was manufactured with the desired mechanical properties, we conducted a vibration test in accordance with ASTM E1876: *Standard Test Method for Dynamic Young's Modulus, Shear Modulus, and Poisson's Ratio by Impulse Excitation of Vibration* [56]. Using this standard, also called the resonance method, one can easily determine Young's modulus based on the fundamental resonant frequency, the geometrical dimensions, and the mass (or density) of the specimens [57].

Fig. B.1 illustrates the experimental setup used to measure the STS 316L rectangular specimen, which was fabricated using a metal additive manufacturing process. To replicate the test schematic presented in Fig. B.1(a), we used a reference microphone (Type 4190; Brüel & Kjær) as the receiver, a modal hammer (Model 2302; Endevco) as the impulser, and a signal analyzer (SR 785; Stanford Research Systems) for post-processing the acoustic signals radiated from the specimen. The designed dimensions of the test specimen are $L = 125\,\text{mm}$, $b = 30\,\text{mm}$, $t = 5\,\text{mm}$, satisfying the dimension ratio criteria: $L/t = 25 > 20$, $b/L = 0.24 < 0.3$, $b/t = 6 < 10$. The measured dimensions of the fabricated specimen are $L = 125.4\,\text{mm}$, $b = 29.75\,\text{mm}$, $t = 5.11\,\text{mm}$. We conducted the impact test and as depicted in Fig. B.1, we identified three fundamental modes within the measurement range: two flexural modes and one torsional mode. Based on calculation formulas using Ref. [56], we determined that Young's modulus, shear modulus, and Poisson's ratio of the fabricated specimen are 205.4 GPa, 71.55 GPa, and 0.43, respectively. Additionally, from the volume measurement, the density was found to be 7886 $\text{kg} \cdot \text{m}^{-3}$. These results suggest that the fabricated material exhibits properties closely matching the desired specifications.

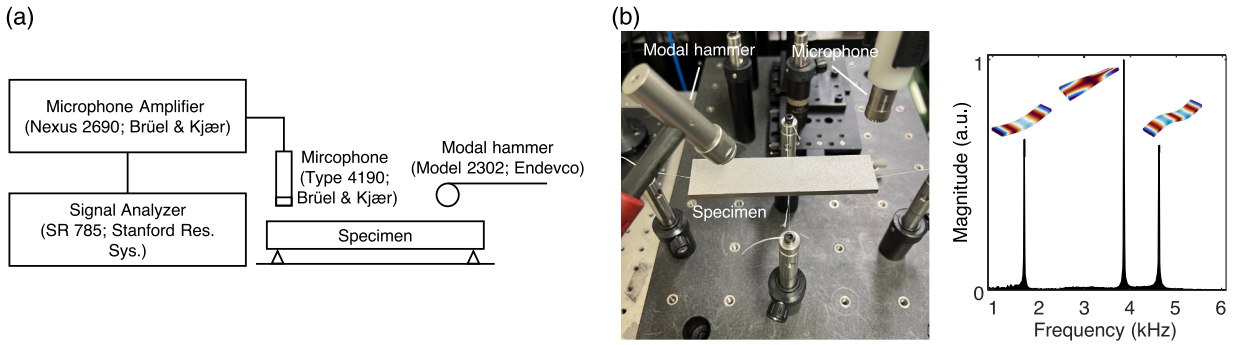

Fig. B.1. Mechanical testing of the test specimen. (a) Schematic of the setup for modal testing. The specimen is excited by a modal hammer, and the radiated sound waves from the specimen are collected by the microphone. (b) Photograph of the experimental setup and measured fast Fourier transform (FFT) data. Each peak in the measured FFT corresponds to the resonance frequencies of the three fundamental modes: first flexural, first torsional, and second flexural, respectively.

Appendix C. Surface roughness of the fabricated sample

To quantitatively assess the surface quality of the fabricated structure, we employed confocal laser scanning microscopy. As shown in Fig. C.1, height profiles were extracted along five randomly selected vertical lines (blue) and five horizontal lines (red). The arithmetic mean surface roughness (R_a) calculated from these ten scans was 8.23 μm. Surface roughness may affect the development

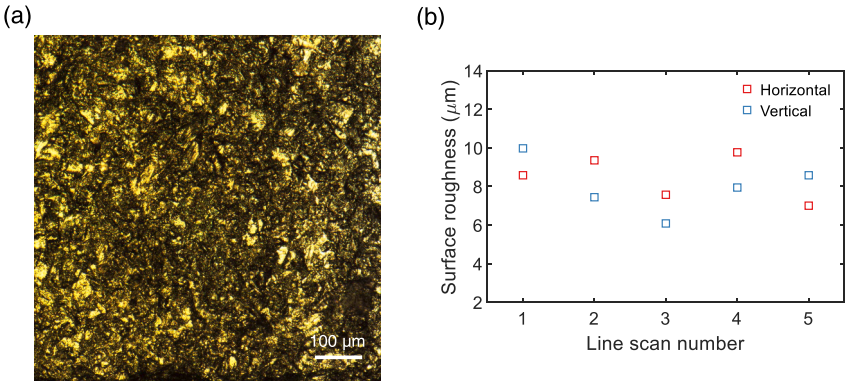

Fig. C.1. Surface roughness measurements. (a) Confocal microscopy image of the fabricated surface, with a 100 μm scale bar. (b) Extracted line profiles along five horizontal (red) and vertical (blue) directions. The average R_a value across all measurements is 8.23 μm. (For interpretation of the references to colour in this figure legend, the reader is referred to the web version of this article.)

of viscous and thermal boundary layers at the fluid-solid interface, thereby introducing attenuation due to boundary-layer dissipation. Such visco-thermal effects become significant when the characteristic channel width is within two orders of magnitude of the boundary-layer thickness [58–60]. The viscous and thermal boundary-layer thicknesses are given by:

$$\delta_v = \sqrt{\frac{2\mu}{\omega\rho_0}}, \qquad \delta_t = \frac{\delta_v}{\sqrt{\mathrm{Pr}}} \tag{C.1}$$

where μ is the dynamic viscosity of water, $\omega = 2\pi f$ is the angular frequency, ρ_0 is the water density, and Pr is the Prandtl number.

At our maximum operating frequency of $f = 35$ kHz, the viscous boundary-layer thickness is approximately $\delta_v \approx 3.2$ μm. Given that the narrowest channel width in the unit cell is 4 mm, the ratio between the viscous boundary layer and the channel width becomes:

$$\Lambda = \frac{\delta_v}{2r_{n,i}} \approx \frac{3.2\times10^{-6}}{0.004} \approx 8\times10^{-4}. \tag{C.2}$$

This result shows that the boundary layers are nearly three orders of magnitude smaller than the structure's critical dimensions. Additionally, the measured surface roughness is below 10 μm, which is also approximately three orders of magnitude smaller than the channel width. Therefore, one can expect that visco-thermal attenuation effects caused by surface roughness will remain negligible.

Surface roughness may also induce unwanted scattering effects, diminishing the coherent (specular) field and generating diffuse components. When the roughness amplitude is small compared to the wavelength, this effect can be analyzed using small perturbation theory (SPT) [61,62]. The key criterion for SPT applicability is the Rayleigh parameter:

$$P = \frac{2\pi\sigma}{\lambda}, \tag{C.3}$$

where σ is the surface roughness. For our system, using $\sigma \approx 8$ μm and $\lambda_{min} \approx 43$ mm, the Rayleigh parameter becomes $P \approx 1.2\times10^{-3} \ll 1$.

Under SPT, the scattered intensity in non-specular directions scales with P^2, i.e.,

$$\left(\frac{2\pi\sigma}{\lambda}\right)^2 \approx 1.4\times10^{-6}. \tag{C.4}$$

This serves as a multiplicative factor for the incident intensity [61] and is well below the detection threshold. This analysis confirms that the contribution of surface roughness to acoustic scattering is negligible under the operating conditions of our system. We note that in the high-frequency ultrasonic regime (hundreds of kHz to MHz), where λ becomes comparable to σ, roughness-induced effects become increasingly prominent and should be treated with more rigorous modeling. For the current low-frequency implementation, however, such effects can be neglected.

Appendix D. Additional experimental results

In Fig. D.1(a), we present the phase distributions of plane waves propagating without the lens at different frequencies (20, 25, 30, 33, and 35 kHz). These results confirm the uniform wavefront propagation of the incident waves. Fig. D.1(b) shows the measured 1D PSFs at 20 kHz for incidence angles of 90°, 180°, and 270°.

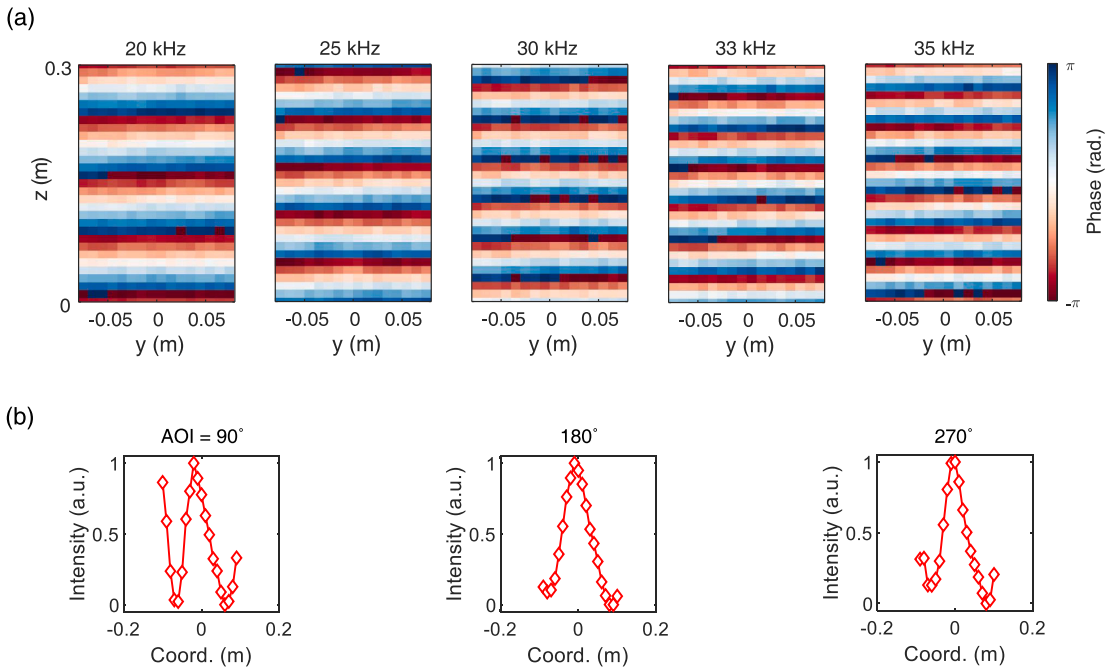

Fig. D.1. Additional experimental results. (a) Phase distributions of plane wave propagation without the lens at different frequencies. (b) Measured one-dimensional intensity profiles at 20 kHz for incidence angles of 90˚, 180˚, and 270˚, respectively.

References

[1] I.F. Akyildiz, D. Pompili, T. Melodia, Underwater acoustic sensor networks: research challenges, Ad Hoc Netw. 3 (3) (2005) 257–279. https://doi.org/10.1016/j.adhoc.2005.01.004

[2] E. Felemban, F.K. Shaikh, U.M. Qureshi, A.A. Sheikh, S.B. Qaisar, Underwater sensor network applications: a comprehensive survey, Int. J. of Distrib. Sens. Netw. 11 (11) (2015) 896832. https://doi.org/10.1155/2015/896832

[3] A. Elfes, Sonar-based real-world mapping and navigation, IEEE J. Robot. Autom. 3 (3) (1987) 249–265. https://doi.org/10.1109/JRA.1987.1087096

[4] M. André, M. Van Der Schaar, S. Zaugg, L. Houégnigan, A.M. Sánchez, J.V. Castell, Listening to the deep: live monitoring of ocean noise and cetacean acoustic signals, Mar. Pollut. Bull. 63 (1–4) (2011) 18–26. https://doi.org/10.1016/j.marpolbul.2011.04.038

[5] J.M. Hovem, Underwater acoustics: propagation, devices and systems, J. Electroceram. 19 (2007) 339–347. https://doi.org/10.1007/s10832-007-9059-9

[6] C.H. Sherman, J.L. Butler, Transducers and arrays for underwater sound, 4, Springer, 2 edition, 2016. https://doi.org/10.1007/978-3-319-39044-4

[7] S.S. Afzal, W. Akbar, O. Rodriguez, M. Doumet, U. Ha, R. Ghaffarivardavagh, F. Adib, Battery-free wireless imaging of underwater environments, Nat. Commun. 13 (2022) 5546. https://doi.org/10.1038/s41467-022-33223-x

[8] B. Assouar, B. Liang, Y. Wu, Y. Li, J.-C. Cheng, Y. Jing, Acoustic metasurfaces, Nat. Rev. Mater. 3 (12) (2018) 460–472. https://doi.org/10.1038/s41578-018-0061-4

[9] B. Oh, K. Kim, D. Lee, J. Rho, Engineering metalenses for planar optics and acoustics, Mater. Today Phys. 39 (2023) 101273. https://doi.org/10.1016/j.mtphys.2023.101273

[10] T. Vasileiadis, J. Varghese, V. Babacic, J. Gomis-Bresco, D. Navarro Urrios, B. Graczykowski, Progress and perspectives on phononic crystals, J. Appl. Phys. 129 (16) (2021) 160901. https://doi.org/10.1063/5.0042337

[11] D. Lee, B. Oh, J. Park, S.-W. Moon, K. Shin, S.-M. Kim, J. Rho, Wide field-of-hearing metalens for aberration-free sound capture, Nat. Commun. 15 (1) (2024) 3044. https://doi.org/10.1038/s41467-024-47050-9

[12] X. He, Z. Ren, Y. Hu, H. Zuo, Y. Li, M. Chen, H.-W. Dong, D. Fang, Overflow elastic metasurfaces for underwater high-pressure-resistant acoustic wavefront control, J. Sound Vib. 607 (2025) 119074. https://doi.org/10.1016/j.jsv.2025.119074

[13] W. Kim, B. Oh, J. Rho, W. Moon, An accurate measurement of parametric array using a spurious sound filter topologically equivalent to a half-wavelength resonator, Appl. Acoust. 240 (2025) 110910. https://doi.org/10.1016/j.apacoust.2025.110910

[14] L. Geng, X. Kong, J. Tang, H.-Y. Xiao, C.-D. He, Y.-Y. Liu, Acoustic sensing enhancement and directional acoustic localization based on nonlinear compact gradient coiled metamaterials, J. Sound Vib. 625 (2026) 119586. https://doi.org/10.1016/j.jsv.2025.119586

[15] N. Gao, J. Guo, M. Wang, D. Qin, X. Liang, Z. Zhang, G. Pan, Achieving precise prediction of sound absorption performance for composite acoustic metamaterials utilizing machine learning, J. Sound Vib. 620 (2026) 119469. https://doi.org/10.1016/j.jsv.2025.119469

[16] J. Yang, P.-S. Ma, Harnessing diffraction with metamaterial noise barriers for enhanced sound attenuation, Mater. Horiz. 13 (2026) 3419–3430. https://doi.org/10.1039/D5MH02051D

[17] W. Kim, B. Oh, W. Moon, J. Rho, Dual-domain metamaterials co-integrated with a compact ultrasonic transducer for highly directional audio generation, Nat. Commun. (2026). https://doi.org/10.1038/s41467-026-73604-0

[18] E. Dong, P. Cao, J. Zhang, S. Zhang, N.X. Fang, Y. Zhang, Underwater acoustic metamaterials, Nat. Sci. Rev. 10 (6) (2023) nwac246. https://doi.org/10.1093/nsr/nwac246

[19] E. Romero-Vivas, B. Leon-Lopez, Analogy of the dolphin jaw to a metamaterial leaky wave antenna for sound directional detection, J. Sound Vib. 604 (2025) 118987. https://doi.org/10.1016/j.jsv.2025.118987

[20] H.-T. Zhou, M. Jiang, J.-H. Zhu, Y. Li, Q. Li, Y.-F. Wang, C.-W. Qiu, Y.-S. Wang, Underwater scattering exceptional point by metasurface with fluid-solid interaction, Adv. Funct. Mater. 34 (37) (2024) 2404282. https://doi.org/10.1002/adfm.202404282

[21] C.-Y. Li, H.-T. Zhou, X.-S. Li, Y.-F. Wang, Y.-S. Wang, Janus metasurface for underwater sound manipulation, Adv. Funct. Mater. 34 (42) (2024) 2408572. https://doi.org/10.1002/adfm.202408572

[22] S. Qu, N. Gao, A. Tinel, B. Morvan, V. Romero-García, J.-P. Groby, P. Sheng, Underwater metamaterial absorber with impedance-matched composite, Sci. Adv. 8 (20) (2022) eabm4206. https://doi.org/10.1126/sciadv.abm4206
[23] D. Lee, Y. Jang, J. Park, I.S. Kang, J. Li, J. Rho, Underwater stealth metasurfaces composed of split-orifice–conduit hybrid resonators, J. Appl. Phys. 129 (10) (2021) 105103. https://doi.org/10.1063/5.0042246
[24] T. Yang, Z. Lin, T. Yang, Experimental evidence of high-efficiency nonlocal waterborne acoustic metasurfaces, Adv. Eng. Mater. 25 (1) (2023) 2200805. https://doi.org/10.1002/adem.202200805
[25] L. Zhao, C. Bi, H. Huang, Q. Liu, Z. Tian, A review of acoustic Luneburg lens: physics and applications, Mech. Syst. Signal Process. 199 (2023) 110468. https://doi.org/10.1016/j.ymssp.2023.110468
[26] R.K. Luneburg, Mathematical Theory of Optics, University of California Press, 1966. https://doi.org/10.2307/jj.8501483
[27] A. Allam, K. Sabra, A. Erturk, 3D-printed gradient-index phononic crystal lens for underwater acoustic wave focusing, Phys. Rev. Appl. 13 (6) (2020) 064064. https://doi.org/10.1103/PhysRevApplied.13.064064
[28] J.-W. Kim, G. Hwang, S.-J. Lee, S.-H. Kim, S. Wang, Three-dimensional acoustic metamaterial Luneburg lenses for broadband and wide-angle underwater ultrasound imaging, Mech. Syst. Signal Process. 179 (2022) 109374. https://doi.org/10.1016/j.ymssp.2022.109374
[29] Y. Xie, Y. Fu, Z. Jia, J. Li, C. Shen, Y. Xu, H. Chen, S.A. Cummer, Acoustic imaging with metamaterial Luneburg lenses, Sci. Rep. 8 (1) (2018) 16188. https://doi.org/10.1038/s41598-018-34581-7
[30] Z. Li, S. Yang, D. Wang, H. Shan, D. Chen, C. Fei, M. Xiao, Y. Yang, Focus of ultrasonic underwater sound with 3D printed phononic crystal, Appl. Phys. Lett. 119 (7) (2021) 073501. https://doi.org/10.1063/5.0058415
[31] C. Lu, R. Yu, Q. Ma, K. Wang, J. Wang, D. Wu, GRIN metamaterial generalized Luneburg lens for ultra-long acoustic jet, Appl. Phys. Lett. 118 (14) (2021) 144103. https://doi.org/10.1063/5.0044436
[32] J.-W. Kim, S.-J. Lee, J.-Y. Jo, S. Wang, S.-H. Kim, Acoustic imaging by three-dimensional acoustic Luneburg meta-lens with lattice columns, Appl. Phys. Lett. 118 (9) (2021) 091902. https://doi.org/10.1063/5.0037600
[33] G. Kim, C.M. Portela, P. Celli, A. Palermo, C. Daraio, Poroelastic microlattices for underwater wave focusing, Extreme Mech. Lett. 49 (2021) 101499. https://doi.org/10.1016/j.eml.2021.101499
[34] S.-J. Lee, J.-W. Kim, S.-H. Kim, D. Lee, B. Oh, J. Rho, G. Hwang, Underwater sound focusing via quasi-three-dimensional gradient-index lens, Phys. Rev. Appl. 23 (6) (2025) 064057. https://doi.org/10.1103/5z2y-d2c3
[35] S. Tong, C. Ren, 3D underwater acoustic Luneburg lens based on gradient face-centered-cubic phononic crystals, Appl. Phys. Lett. 123 (3) (2023) 031703. https://doi.org/10.1063/5.0145179
[36] L. Quan, Y. Ra'di, D.L. Sounas, A. Alù, Maximum willis coupling in acoustic scatterers, Phys. Rev. Lett. 120 (25) (2018) 254301. https://doi.org/10.1103/PhysRevLett.120.254301
[37] H. Esfahlani, Y. Mazor, A. Alù, Homogenization and design of acoustic Willis metasurfaces, Phys. Rev. B 103 (5) (2021) 054306. https://doi.org/10.1103/PhysRevB.103.054306
[38] M.B. Muhlestein, C.F. Sieck, P.S. Wilson, M.R. Haberman, Experimental evidence of Willis coupling in a one-dimensional effective material element, Nat. Commun. 8 (1) (2017) 15625. https://doi.org/10.1038/ncomms15625
[39] A. Melnikov, Y.K. Chiang, L. Quan, S. Oberst, A. Alù, S. Marburg, D. Powell, Acoustic meta-atom with experimentally verified maximum Willis coupling, Nat. Commun. 10 (1) (2019) 3148. https://doi.org/10.1038/s41467-019-10915-5
[40] X. Su, A.N. Norris, Retrieval method for the bianisotropic polarizability tensor of Willis acoustic scatterers, Phys. Rev. B 98 (17) (2018) 174305. https://doi.org/10.1103/PhysRevB.98.174305
[41] V.S. Asadchy, A. Díaz-Rubio, S.A. Tretyakov, Bianisotropic metasurfaces: physics and applications, Nanophotonics 7 (6) (2018) 1069–1094. https://doi.org/10.1515/nanoph-2017-0132
[42] C.E. Kriegler, M.S. Rill, S. Linden, M. Wegener, Bianisotropic photonic metamaterials, IEEE J. Sel. Top. Quantum Electron. 16 (2) (2010) 367–375. https://doi.org/10.1109/JSTQE.2009.2020809
[43] D.C. Calvo, A.L. Thangawng, M. Nicholas, C.N. Layman, Thin Fresnel zone plate lenses for focusing underwater sound, Appl. Phys. Lett. 107 (1) (2015) 014103. https://doi.org/10.1063/1.4926607
[44] Z. Cai, S. Zhao, Z. Huang, Z. Li, M. Su, Z. Zhang, Z. Zhao, X. Hu, Y.-S. Wang, Y. Song, Bubble architectures for locally resonant acoustic metamaterials, Adv. Funct. Mater. 29 (51) (2019) 1906984. https://doi.org/10.1002/adfm.201906984
[45] M. Pan, Y. Fu, M. Zheng, H. Chen, Y. Zang, H. Duan, Q. Li, M. Qiu, Y. Hu, Dielectric metalens for miniaturized imaging systems: progress and challenges, Light Sci. Appl. 11 (1) (2022) 195. https://doi.org/10.1038/s41377-022-00885-7
[46] Z. Liu, X. Zhang, Y. Mao, Y.Y. Zhu, Z. Yang, C.T. Chan, P. Sheng, Locally resonant sonic materials, Science 289 (5485) (2000) 1734–1736. https://doi.org/10.1126/science.289.5485.1734
[47] G. Ma, P. Sheng, Acoustic metamaterials: from local resonances to broad horizons, Sci. Adv. 2 (2) (2016) e1501595. https://doi.org/10.1126/sciadv.1501595
[48] S. Kim, J. Choi, H.M. Seung, I. Jung, K.H. Ryu, H.-C. Song, C.-Y. Kang, M. Kim, Gradient-index phononic crystal and Helmholtz resonator coupled structure for high-performance acoustic energy harvesting, Nano Energy 101 (2022) 107544. https://doi.org/10.1016/j.nanoen.2022.107544
[49] Y. Jang, B. Oh, E. Kim, J. Rho, Bidirectional asymmetric frequency conversion in nonlinear phononic crystals, Phys. Rev. Lett. 135 (3) (2025) 036603. https://doi.org/10.1103/3n97-7kmd
[50] M.J.A. Smith, P.A. Cotterill, D. Nigro, W.J. Parnell, I.D. Abrahams, Asymptotics of the meta-atom: plane wave scattering by a single Helmholtz resonator, Phil. Trans. R. Soc. A 380 (2237) (2022) 20210383. https://doi.org/10.1098/rsta.2021.0383
[51] J.-P. Groby, M. Mallejac, A. Merkel, V. Romero-García, V. Tournat, D. Torrent, J. Li, Analytical modeling of one-dimensional resonant asymmetric and reciprocal acoustic structures as Willis materials, New J. Phys. 23 (5) (2021) 053020. https://doi.org/10.1088/1367-2630/abfab0
[52] D.P. Elford, L. Chalmers, F.V. Kusmartsev, G.M. Swallowe, Matryoshka locally resonant sonic crystal, J. Acoust. Soc. Am. 130 (5) (2011) 2746–2755. https://doi.org/10.1121/1.3643818
[53] A.N. Norris, G. Wickham, Elastic Helmholtz resonators, J. Acoust. Soc. Am. 93 (2) (1993) 617–630. https://doi.org/10.1121/1.405481
[54] X. Su, A.N. Norris, C.W. Cushing, M.R. Haberman, P.S. Wilson, Broadband focusing of underwater sound using a transparent pentamode lens, J. Acoust. Soc. Am. 141 (6) (2017) 4408–4417. https://doi.org/10.1121/1.4985195
[55] Y. Ruan, X. Liang, Z. Wang, T. Wang, Y. Deng, F. Qu, J. Zhang, 3-D underwater acoustic wave focusing by periodic structure, Appl. Phys. Lett. 114 (8) (2019). https://doi.org/10.1063/1.5081661
[56] Standard Test Method for Dynamic Young's Modulus, Shear Modulus, and Poisson's Ratio by Impulse Excitation of Vibration, 2022, Accessed: https://doi.org/10.1520/E1876-22
[57] J.-J. Wang, T.-P. Chang, B.-T. Chen, H. Wang, Determination of Poisson's ratio of solid circular rods by impact-echo method, J. Sound Vib. 331 (5) (2012) 1059–1067. https://doi.org/10.1016/j.jsv.2011.10.030
[58] X. Jiang, Y. Li, L. Zhang, Thermoviscous effects on sound transmission through a metasurface of hybrid resonances, J. Acoust. Soc. Am. 141 (4) (2017) EL363–EL368. https://doi.org/10.1121/1.4979682
[59] G.P. Ward, R.K. Lovelock, A. Murray, A.P. Hibbins, J.R. Sambles, J.D. Smith, Boundary-layer effects on acoustic transmission through narrow slit cavities, Phys. Rev. Lett. 115 (4) (2015) 044302. https://doi.org/10.1103/PhysRevLett.115.044302
[60] P.M. Morse, K.U. Ingard, Theoretical Acoustics, Princeton university press, 1986.
[61] J.A. Ogilvy, Theory of Wave Scattering from Random Rough Surfaces, CRC Press, 1991.
[62] L.M. Brekhovskikh, Y.P. Lysanov, Fundamentals of Ocean Acoustics, Springer Science & Business Media, 2006. https://doi.org/10.1007/b97388